VORTEX SHEDDING ENHANCEMENT FOR ENERGY HARVESTING APPLICATIONS IN MINIATURE DEVICES

Dimitrios G. Koubogiannis[1] and Ioannis Bonis[1]

[1]Department of Energy Technology Engineering
Technological Educational Institute of Athens
Agiou Spyridonos Street, 12210 Egaleo, Athens, Greece
e-mails: dkoubog@teiath.gr, ibonis@helpe.gr

Keywords: Flow energy harvesting, vortex shedding enhancement, bluff body.

Abstract. *Millimetre-scale energy harvesting devices are increasingly used in various fields as for example in Wireless Sensor Networks (WSN) that have made a great progress in recent years in many applications. However, their main shortcoming is their limited life of operation unless an effective way to power them (recharge their batteries) is efficiently implemented. In this present paper, micro-energy harvesting from flow (e.g. wind or flow in a pipe) is of interest and, in particular, the exploitation of von Karman vortex street behind bluff bodies in order to cause oscillations to a piezoelectric film and generate the required electrical energy. Numerical simulations are carried out by means of Computational Fluid Dynamics (CFD) on a test case from the literature, in order to study the flow around bluff micro-bodies contained a miniature device. Aiming to enhance vortex shedding, parametric studies corresponding to different bluff body shapes and arrangements are performed. The potential for vortex shedding exploitation in such energy harvesting configurations is assessed.*

1 INTRODUCTION

Wireless sensor networks (WSN) have made a great progress in recent years, in many applications. However, their main shortcoming is their limited life of operation unless an effective way to power them (actually recharge their batteries) is efficiently implemented [1]. WSN are used in industrial process monitoring and control, machine health monitoring, environment monitoring, etc. Energy harvesting for powering WSN is a very attractive state-of-the-art research topic. WSN is just a characteristic application among others where millimetre-scale energy harvesting devices are required. Energy sources offered for micro-energy harvesting are mechanical, electromagnetic, thermal, solar, etc. Miniature pneumatic power systems, i.e. those that convert flow energy into electricity, either use micro-turbines [2],[3] or bluff bodies [4]. In the former case, precise fabrication of millimetre-scale turbomachinery components is required for efficient energy harvesting, while the latter offers the advantage of simple design and ease of application [4]. The bluff body is installed in the flow on purpose. The flow unsteadiness caused due to the vortex shedding that takes place behind the body for a wide range of Reynolds numbers, provides pressure fluctuations that can be utilized by energy-converting materials, like piezoelectric membranes, to generate electrical power.

Application of the piezoelectric effect for flow energy harvesting by flexible structures exploiting fluid structure interaction phenomena can be found in the literature [5],[6],[7], where various configurations using flexible membranes in combination with bluff bodies are proposed and assessed in either external or internal flows, prototype devices are fabricated and experimentally tested and/or numerical simulations are performed. Some of these studies concern the bluff body shape to be installed in a channel in order to continuously produce significant vortex shedding, the objective being the same like for the design of an effective flow meter [8],[9]. The use of multiple bluff bodies in tandem is an interesting perspective aiming to enhance vortex shedding [10],[11]. A good and compact literature review on the above issues can be found in [4]. However, further research is still required, since the power produced by such devices is often not enough for practical use [4].

In the present work, some preliminary parametric studies and findings on vortex shedding exploitation in energy harvesting applications are presented. A miniature pneumatic energy generating device proposed in [4] is considered as test case. One or two bluff bodies in tandem are installed in a channel causing vortex shedding, pressure fluctuations and unsteady forces to a flexible diaphragm located at the upper wall of the channel. The diaphragm is connected to a piezoelectric film that is vibrated and converts mechanical energy to electrical. The flow around bluff micro-bodies of various shapes contained in the miniature device is numerically simulated by means of CFD, in order to predict and compare the related von Karman vortex street and pressure fluctuation characteristics (frequency and amplitude). Results are presented and discussed, the potential for exploiting vortex shedding in energy harvesting applications is assessed and suggestions for further research are made.

2 TEST CASE DESCRIPTION

2.1 Flow domain geometry

Figure 1 presents the two small triangles installed in a flow channel. Above the two bluff bodies a flexible diaphragm has been installed. Under the action of the unsteady flow pressure due to vortex shedding, this diaphragm causes vibrations to a piezoelectric film connected to it; the latter converts mechanical energy to electrical. Such a device has been fabricated, as well as experimentally and numerically tested in [4], where two configurations, using one or two triangles in tandem have been comparatively studied, since the greater the pressure fluctuation amplitude on the diaphragm the better the performance of the device.

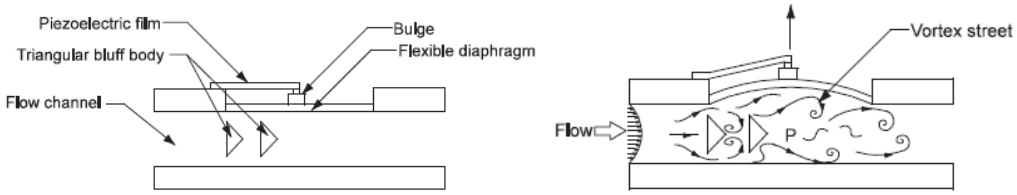

Figure 1. Miniature energy harvesting device using two triangles in tandem (from [4]).

The flow domain used for the numerical simulations in the present study is shown in Figure 2. The dimensions used in [4] have also been implemented herein. The channel length is L=77.06D and its height is H=3.76D, where D=4.25mm is the width (diameter) of the bluff body. The flexible diaphragm is located on the upper wall at a distance of 23.53D from the inlet. The length of the diaphragm is 4.47D and after it, a wall length of 44.59D follows up to the outlet of the channel. The upper and lower boundaries of the channel are treated as solid walls, the inlet is at the left boundary of the domain and the outlet is at the right one (Figure 2). In Figure 2, S is the center of the diaphragm, while BB1 and BB2 denote the sections where the bases of the first (BB1) and the second (BB2) bluff bodies, respectively, are installed. In the configurations used in [4], the bluff body was an isosceles triangle, the base of which faced the incoming flow (Figure 2).

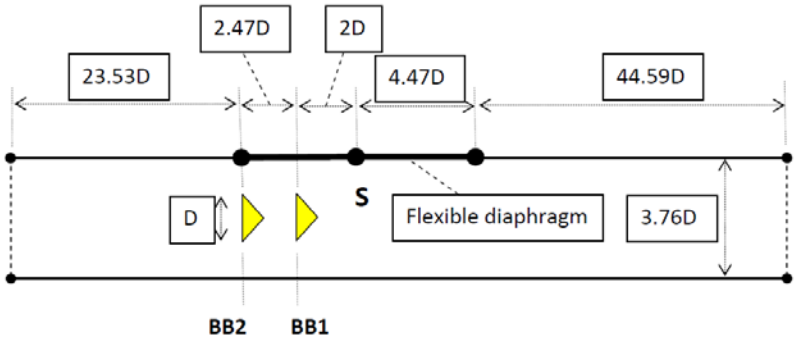

Figure 2. The computational flow domain used for the numerical simulations.

2.2 Different bluff body configurations and test cases

In the present study, apart from the isosceles triangle (triangle-base) mentioned above, some other bluff body shapes were used in the simulations, namely the same isosceles triangle installed in a way that its sharp edge faces the incoming flow (triangle-sharp), i.e. the triangle of the baseline configuration turned by 180^o, a semi-circle with its circular arc shaped side faceing the incoming flow, an orthogonal triangle turned 35^o with respect to the vertical direction and pointing to the diaphragm (triangle-turned), as well as a rectangular. In each case, two configurations were tested, containing one or two bodies of the corresponding shape. Whenever one bluff body was used, this was located at section BB1. In case of two bluff bodies, the second one was located in front of the first at section BB2 (Figure 1). Table 1 presents the nomenclature and a brief description of the different cases simulated in the present study. The corresponding geometries are shown in Figure 3, where focused views of the computational grids in the vicinity of the bluff bodies are presented. In all cases but the last one (F2), the width D of the bluff body was the same, corresponding for the channel under consideration to a blockage ratio BR= D/H=0.27. The last case in Table 1 is the same like A2, where the bluff body width D has been modified from 4.25mm to 5.274 in order to achieve a blockage BR=0.33.

Incoming flow on		triangle-base	triangle-sharp	semi-circle	triangle-turned	rectangle	triangle base BR=0.33
Number of bodies	1	A1	B1	C1	D1	---	---
	2	A2	B2	C2	D2	E2	F2

Table 1: Nomenclature and description of cases simulated in the present study.

3 CFD SIMULATIONS

The ANSYS FLUENT commercial CFD software was used for the numerical simulations, while the necessary geometry modeling and grid generation tasks were accomplished by means of the relevant ANSYS software modules.

3.1 Governing equations and numerical solution

The steady two-dimensional (2D) Reynolds-averaged incompressible Navier-Stokes equations (continuity and momentum equations) were solved. The eddy-viscosity assumption for the turbulence modeling was considered and the realizable variant of the k-ε two-equation model that ensuring that only physically realistic (realizable) viscous stresses will arise during the simulations was used. The finite volume method was implemented, in conjunction with the SIMPLE pressure correction scheme. Second order accuracy was used for the convective terms of the mean flow equations, while first order was used for the turbulence model ones. Transient solution of the governing equations was sought by means of first order Euler scheme in time with a constant physical time step. 2D grids of triangular elements were created for the simulated cases. Inlet velocity was prescribed at the inlet boundary. Zero pressure was set to the outlet boundary. No slip conditions were used for velocity at walls. Wall functions were implemented to model velocity profiles at wall boundaries. In particular, the enhanced wall treatment version provided by the software was used, that automatically switches to a two-layer low Reynolds approach and resolves the boundary layer up to the wall wherever a small value of y+ (e.g. of the order of 10 or less) is met.

3.2 Grid generation

2D grids consisting of triangular elements were created to discretize the flow domain described in Figure 2 and containing the corresponding bluff body or bodies in each of the cases of Table 1. Figure 4 presents some pictures of these grids in the vicinity of the bluff bodies. The mesh generated for case B2 consists of 11244 triangles / 5970 nodes and this is the order of magnitude of the grid size for all cases.

3.3 Flow conditions and CFD parameters

Air was used as the working fluid in the channel. An inlet velocity V_{in}=20.7m/s was considered [4]. Air density was ρ=1.225kg/m^3, the dynamic viscosity coefficient of air was $\mu=1.789\times10^{-5}$Pa.s and as characteristic length of the flow, the width of the bluff body D=4.25mm=0.00425m was considered, giving a Reynolds number $Re_D=\rho V_{in}D/\mu$=6024 that dictates turbulent flow. The turbulence inlet conditions were prescribed by providing turbulence intensity I_t and turbulent length scale l_t. The latter was estimated for fully developed flow by the formula $l_t=0.07L_c$ (where L_c is the duct inlet size or the obstacle size if any). Thus, L_c=D and l_t=0.3mm. Turbulence intensity was computed by $I_t=0.16(Re_D)^{-1/8}$=0.054=5.4%. To justify the use of the enhanced wall treatment version of the wall functions, the value of y^+ was computed for the various simulations and was found to be in the range 15÷75 for the upper and lower walls of the flow domain and about 1÷7 at the vicinity of the bluff body walls. Thus, the use of the enhanced wall treatment version is justified, since for the use of standard wall functions y^+ should be ideally in the range 30÷300.

Concerning the flexible diaphragm, this was considered to be rigid wall in the simulations. Thus, fluid structure interaction phenomena were ignored. The assumption behind this is that the diaphragm has small inertia and is able to oscillate with the frequency of vortex shedding, the piezoelectric film is strained laterally following the vibrations of the diaphragm and, according to the piezoelectric phenomenon, produces electrical power. By ignoring the fluid structure interaction phenomena, the displacement of the fluid due to the diaphragm motion is ignored and feedback effects from the diaphragm to the flow are neglected. Although the actual geometry is 3D, 2D simulations along the symmetry plane of the channel were performed in the present study.

A constant time step was used in physical time. Estimating the convective time by $T_c=D/V_{in}=2.05\times10^{-4}$s, a physical time step $\Delta t=(0.05)T_c=10^{-5}$s (or 0.01ms) was used in the unsteady simulations as in [4]. At each case, 8ms in physical time (800 time steps) were simulated starting from an ambient initial velocity field.

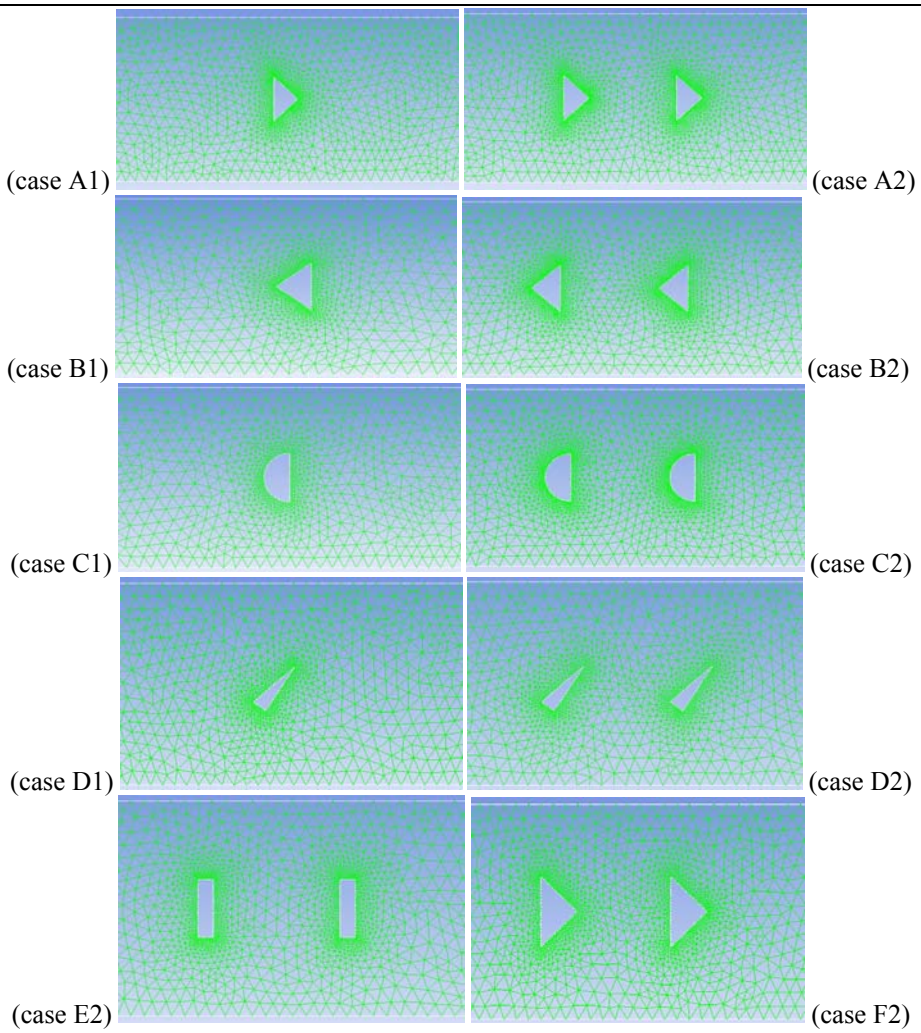

Figure 3. Focused view of the grid in the vicinity of the bluff bodies.

4 RESULTS AND DISCUSSION

4.1 Vortex shedding and velocity field

Figure 4 presents the instantaneous velocity isolines at time t=8ms for the various cases. In these pictures, asymmetries in the flow field can be observed due to vortex shedding. In any case, periodicity was established after an initial transient stage of about 5ms, as it is shown in Figure 5 for the pressure evolution on the center S of the diaphragm for cases A1 and A2. According to this figure, the period of vortex shedding is about 100 physical time steps or 1ms. Thus, the Strouhal number (nondimensional frequency) is $St=fD/V_{in}=0.2$.

4.2 Unsteady pressure evolution

The unsteady pressure evolution in time was computed and compared for each case at the center of the diaphragm S (see Figure 2). The pressure fluctuation amplitude, i.e. p_{max}-p_{min} in a vortex shedding period, was considered as an indicative quantity of the vortex shedding severity.

Figure 6(left) presents depicts the pressure evolution at the center S of the diaphragm for the cases A1, B1, C1, D1 containing one bluff body. It is evident that the case A1, in which the base of the triangle faces the incoming flow, causes the greater pressure amplitude at S. The same triangle pointing the incoming flow with its sharp edge, produces an evolution of smaller amplitude, while the other two bodies, namely the semi-circle and the orthogonal triangle turned 35^o cause variations of much smaller amplitudes. Figure 6(right) presents the corresponding pressure evolutions and for the cases A2, B2, C2, D2, E2 containing two bluff bodies. Again, the use of triangles facing the incoming flow with their base (case A2) is the most effective in enhancing vortex shedding. The two rectangles in tandem produce the next significant pressure variation of the amplitude and they are followed by the shapes of cases B2, C2 and D2.

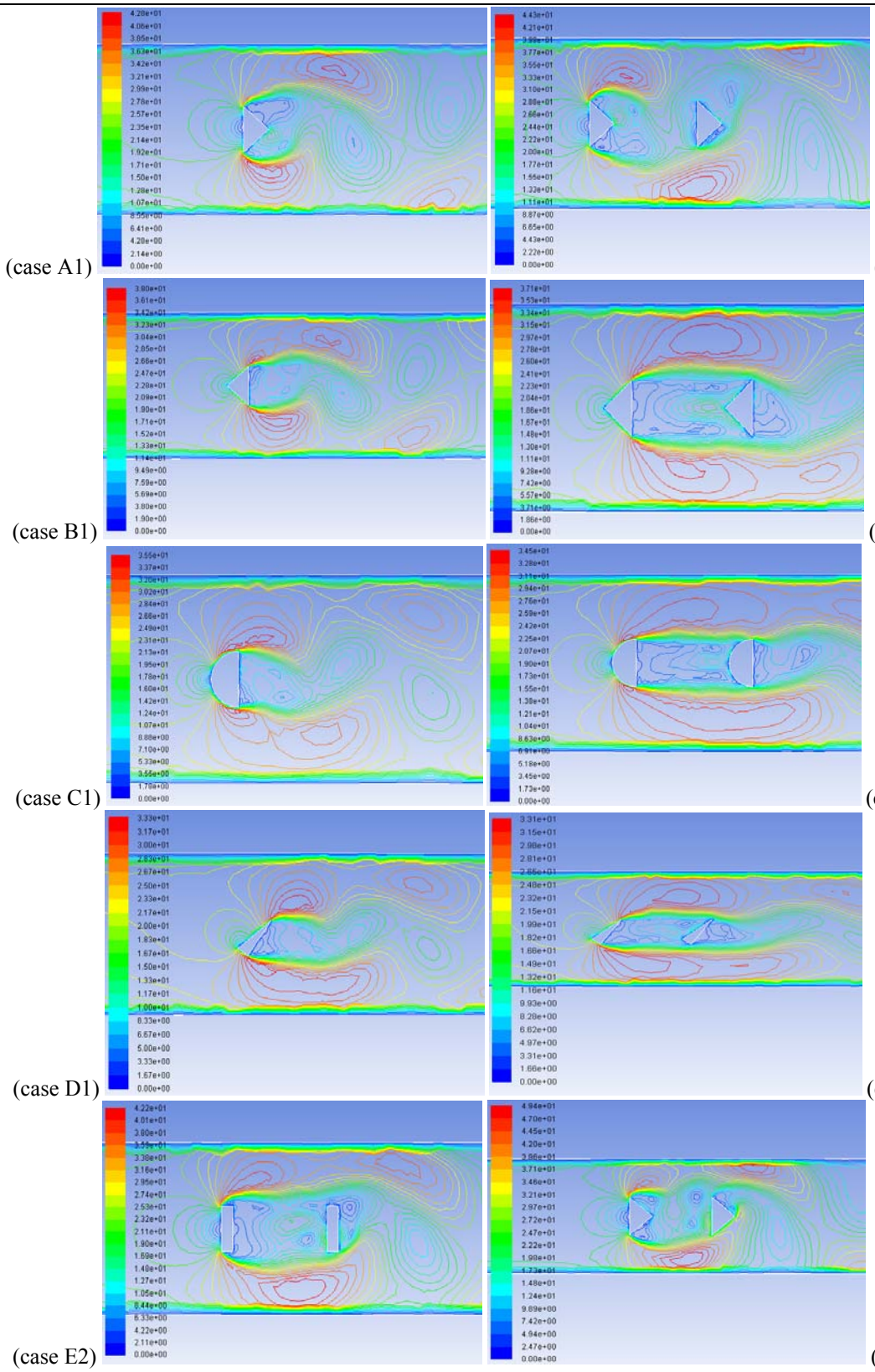

(case A1) (case A2)

(case B1) (case B2)

(case C1) (case C2)

(case D1) (case D2)

(case E2) (case F2)

Figure 4. Instantaneous velocity isolines (at time 8ms) near the bluff bodies.

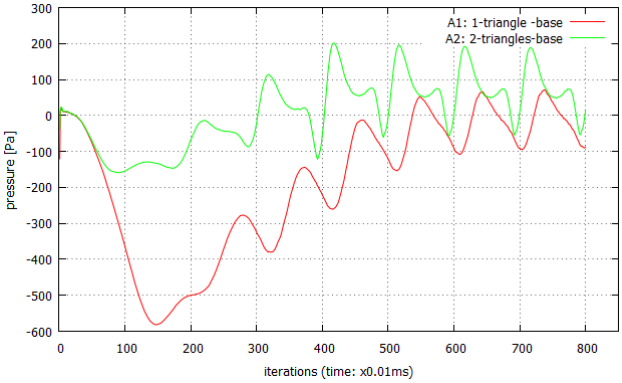

Figure 5. Pressure evolution at the center S of the diaphragm for cases A1 and A2. Periodicity is established after about 5ms in physical time from the beginning of the calculation.

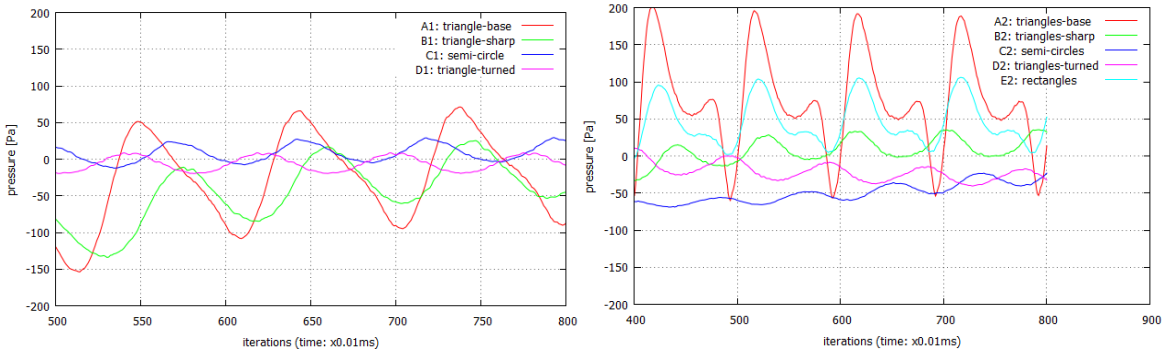

Figure 6. Pressure evolution at the center S of the diaphragm for the cases A1, B1, C1, D1 containing one bluff body (left) and for the cases A2, B2, C2, D2, E2 containing two bluff bodies (right).

Figure 7 presents results for the pressure evolution at the center S of the diaphragm for case A2 by the present study and corresponding results from the literature [4]. As it can be noticed by Figure 7(left), the use of two triangles in tandem (case A2) significantly increases pressure variation amplitude (240 Pa) compared to that (165 Pa) caused by the use of one triangle (case A1). The present results produce pressure evolution curves that are similar with those of [4] shown in Figure 7(right). However, compared to the results of [4] for both cases A1 and A2, the present results predict a little greater pressure amplitudes, namely 165 and 240 Pa instead of 155 and 215 Pa, respectively. Although the same CFD model (FLUENT commercial software) and case parameters have been implemented in [4] and the present study, some differences could be pointed out as an attempt to explain the discrepancies between them. These are the different density of the computational grid (the present one is denser near the bodies compared to the upper and lower walls, while that of [4] is isotropic everywhere), the enhanced wall treatment variant of the wall functions used herein and the inlet values for the k and ε variables (the authors in [4] do not provide y^+ values for their simulations, neither inlet values for k and ε).

Figure 8 presents comparisons of the pressure evolutions at the center S of the diaphragm for the same bluff body shape between the single and dual body configurations for the rest of the cases, namely B1, B2 in Figure 8(left), C1, C2 in Figure 8(center) and D1, D2 in Figure 8(right). A first remark is that all these configurations produce much smaller pressure amplitudes than those of cases A1 and A2. The pressure amplitudes predicted for each case are summarized in Table 2. Other remarks are that in cases C1 and C2 the results are practically the same, i.e. the use of the second body does not affect vortex shedding severity, while in cases B2 and D2, less severe pressure variations are predicted compared to B1 and D1, respectively, i.e. the use of the second body suppresses the variation amplitude instead of enhancing it.

Case	A1	**A2**	B1	B2	C1	C2	D1	D2	E2	F2
Δp[Pa]	165	**240**	75	35	35	35	28	23	100	335

Table 2: Pressure amplitudes predicted at each case.

From what presented above, it is evident that the configuration causing the more severe pressure variations among those tested, are A1 and A2. The use of the second body in the latter significantly enhances vortex shedding compared to the former. However, the studied pressure variations refer to the center of the diaphragm S which has been arbitrarily located at the position described in [4] and adopted herein. Since the diaphragm is

considered as solid wall in the computations, it is interesting to study the pressure variation along various positions along the diaphragm. This means that in the context of considering the diaphragm solid, if greater pressure variations were found at positions other than S, the whole diaphragm should be installed in a way that its center S is located at the position of the maximum pressure variation. Although such an investigation could refer to an extended length on the upper wall, in the present work, some points along the diaphragm at its current position were studied. In particular, 11 positions along the diaphragm were defined for each of the cases containing two bluff bodies in tandem. The definition of the exact locations of these points, denoted by p0, p1,…, p10, along the diaphragm, are schematically described in Figure 9.

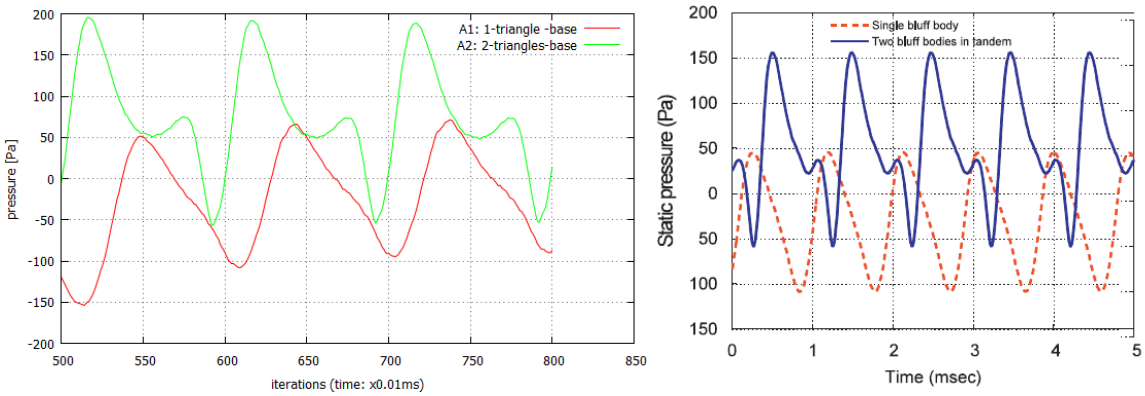

Figure 7. Pressure evolution at S for case A2: present study (left) and from [4] (right).

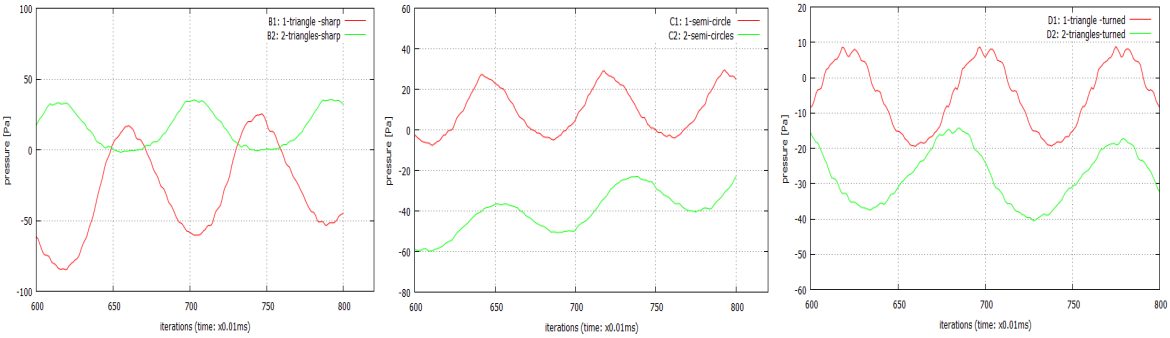

Figure 8. Pressure evolution at S for cases: B1, B2 (left), C1, C2 (center) and D1, D2 (right).

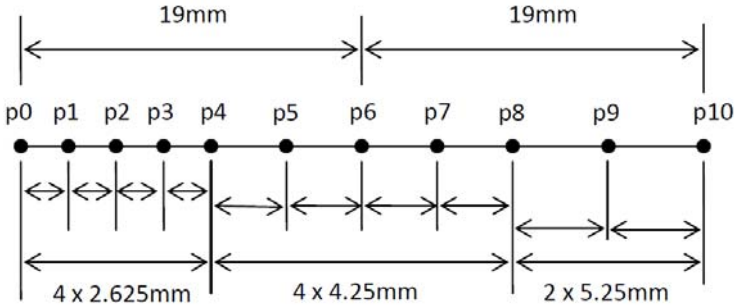

Figure 9. Locations of points p0, p1,…, p10 along the diaphragm, where the pressure evolution was stored for each of the cases containing having two bluff bodies in tandem. Point p6 is the center S of the diaphragm.

The unsteady pressure evolution curves in time that were computed at these 11 points along the diaphragm for case A2 are shown in Figure 10. In order to better understand and study these curves, they are presented in two diagrams. The first of them in Figure 10(left) shows the pressure evolution at points p0,…,p6, namely at the points located to the left of the diaphragm center S (S is identical to point p6). The second one in Figure 10(right) shows the corresponding curves at points p6,…,p10, which are located downstream the diaphragm center S. For the purpose of comparison, in both diagrams the pressure evolution at the diaphragm center S (p6) was considered to be the reference one and has been highlighted (using points along the plot of the corresponding curve). Referring to Figure 10(right), a first remark is that the points located downstream the center S exhibit smaller pressure variation amplitudes than. Thus, the center S should not be placed downstream

its current position. By carefully examining Figure 10(left), it seems that all the points located upstream of S exhibit pressure variation amplitudes that, at a first glance, are comparable to that of S. The pressure amplitudes predicted at each of these points p0,…,p6 are summarized in Table 3. Points p3 and p5 located upstream point S (p6) exhibit a significant increase of the pressure variation amplitude of the order of 46%.

Point	p0	p1	p2	**p3**	p4	**p5**	p6
Δp[Pa]	235	250	245	**355**	280	**350**	240

Table 3: Pressure amplitudes predicted for case A2.

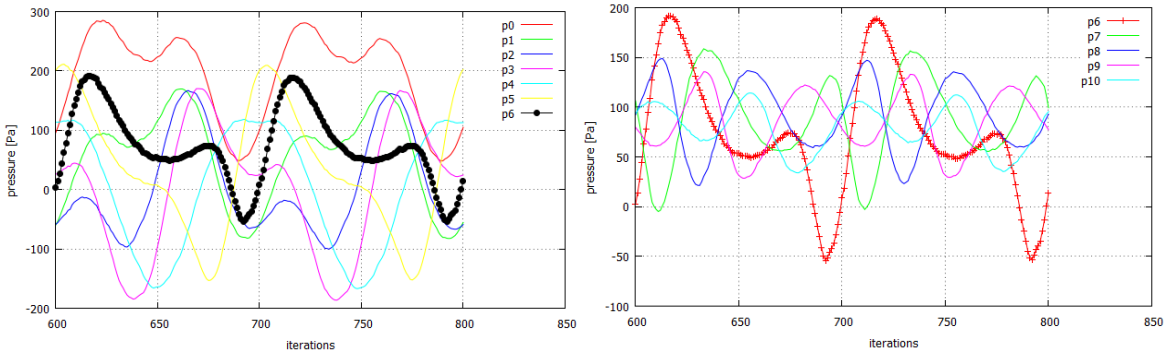

Figure 10. Pressure evolution for case A2 along the diaphragm at points p0,…p6 (left) and p6,…p10 (right).

Based on the main conclusion concerning case A2, i.e. that the maximum pressure variation amplitude is attained at a point upstream the diaphragm center S, similar studies were also performed for cases B2 (Figure 11), C2 and D2 (Figure 12). According to Figure 11, the remarks concerning case B2 are that downstream of S, pressure differences are less than that of S ($\Delta p_{S,B2}$=35 Pa), while upstream of S they are comparable to $\Delta p_{S,B2}$ and, in particular, points p3, p5 exhibit Δp comparable to $\Delta p_{S,B2}$, while the value at point p4 (55 Pa) supersedes it at a percent of 57%.

Figure 12(left) presents the pressure evolution along all the diaphragm at points p0,…,p10 in one diagram for case C2, while Figure 12(right) presents the corresponding results for case D2. In case C2 (2 semi-circles in tandem), all the curves exhibit pressure variation amplitude comparable to that of the center S (35 Pa) and no point, either upstream or downstream of S, exhibits a noteworthy increase. Figure 12(b) presents the corresponding results for case D2. Again, no point downstream of S exhibits greater amplitude, while for p3, p4 and p5 upstream of S, an increase of 117% is predicted (for example for point p4 where the amplitude is 50 Pa compared to the 23 Pa of the center S).

Figure 13 presents similar results for case E2, using two bodies of rectangular shape. In particular, Figure 13(right) shows the pressure variation for points downstream of S, all of them having a smaller value than that of S ($\Delta p_{S,E2}$=100 Pa), while Figure 13(left) shows the corresponding variations for the points upstream of S. Again, the conclusion is the same, i.e. points p3, p4, p5 exhibit a significant increase over $\Delta p_{S,E2}$ (for example for point p4, where the amplitude is 155 Pa, this is of the order of 55%).

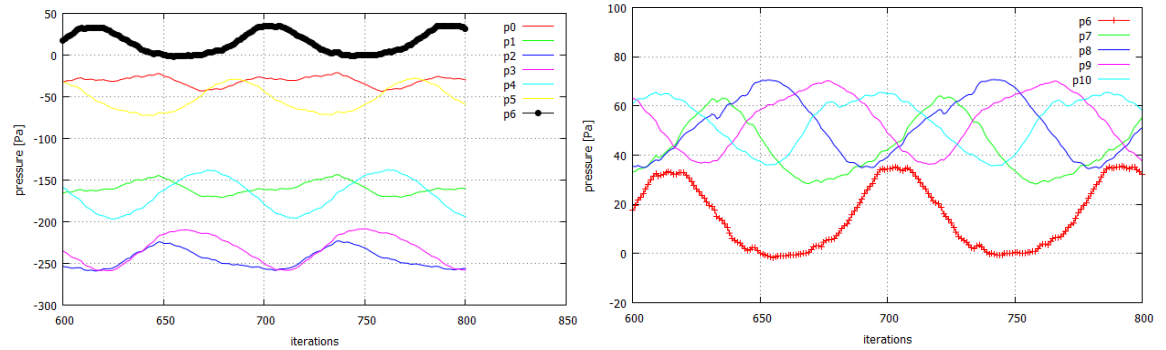

Figure 11. Pressure evolution for case B2 along the diaphragm at points p0,…p6 (left) and p6,…p10 (right).

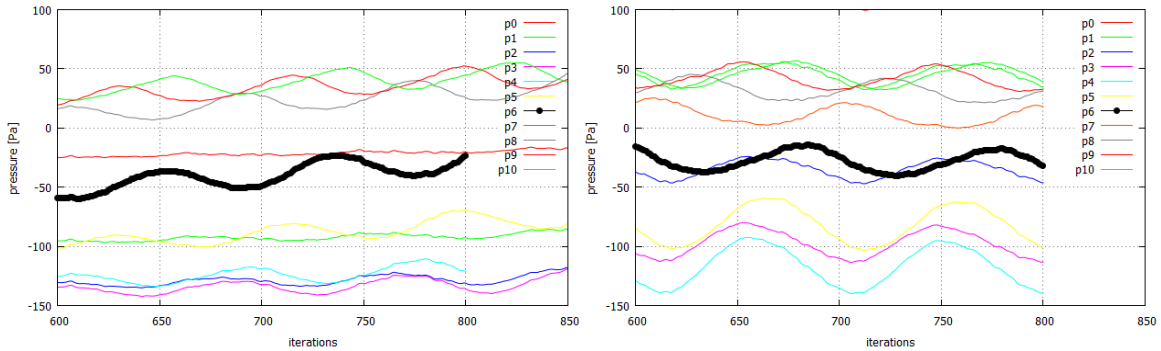

Figure 12. Pressure evolution along the diaphragm at points p0,…p10 for cases C2 (left) and D2 (right).

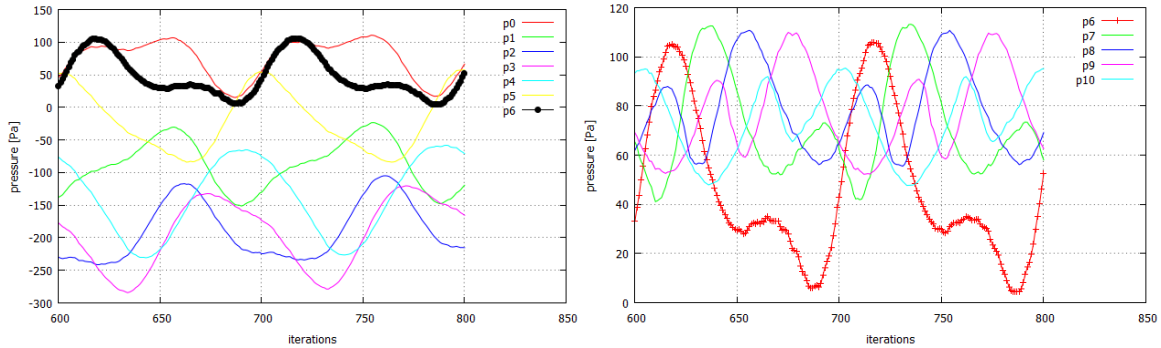

Figure 13. Pressure evolution for case E2 along the diaphragm at points p0,…p6 (left) and p6,…p10 (right).

The main conclusions up to this point are:

- the triangular body shape located as in cases A1 and A2 causes the more severe pressure variations,
- the second body enhances the phenomenon
- the maximum amplitude happens upstream the current position of the center S of the diaphragm.

These findings are in accordance with similar findings and results in the literature [4]. In [9] it is also stated that the maximum pressure variation happens at the point where the minimum absolute pressure is located. This fact seems also to be valid herein, at least in case A2 (Figure 10(left)), where the most significant results have been found.

Furthermore, the blockage ratio BR plays an important role to the pressure variation amplitude, according to literature [8]. By further thinking the previous statement, the velocity in the region near the point where maximum pressure variation happens and pressure is minimum, is maximum. So in order to achieve even smaller pressure and, consequently, greater pressure variation amplitude, we have to achieve greater nearby velocity. The latter can happen by decreasing the flow area. Such a decrease can be achieved in our case by increasing the BR or, equivalently, the width D of the bluff body. In [8] a BR value of 0.30 was experimentally found to be better, while in [4] a BR value of 0.33 was numerically found to cause the greater increase in pressure amplitude for the device under consideration. Besides the above reasoning, in practice, greater values of BR than the optimum may inhibit the vortex shedding phenomenon and lead to its suppression, due to the proximity of walls in smaller distances to the bluff body in this case.

In order to test the above statement for the optimum BR value, the case A2 (exhibiting the best results up to here) was simulated again in a channel with BR=0.33 instead of the original one (that was 0.27) by increasing the triangle base length D from 4.25mm to 5.274mm (case F2 of Table 1). Figure 14 presents the pressure variation results for the different points along the diaphragm. Qualitatively, the conclusions are the same, i.e. upstream the center S the amplitudes are greater and downstream less pronounced, but quantitatively the results are impressive since the increase becomes important enough. Table 4 summarizes the pressure amplitude values for the same points upstream of S for both cases A2 and F2 (similar configurations with BR 0.27 and 0.33, respectively). The greater blockage case F2 exhibits a mean increase of 50% over the amplitudes of case A2.

Point	p0	p1	p2	p3	p4	p5	p6
Δp[Pa], A2	235	250	245	**355**	280	350	240
Δp[Pa], F2	325	390	385	500	470	**525**	335
% increase	38%	56%	57%	41%	**68%**	50%	40%

Table 4: Comparison of pressure variation amplitudes cases A2 and F2 at points upstream of S.

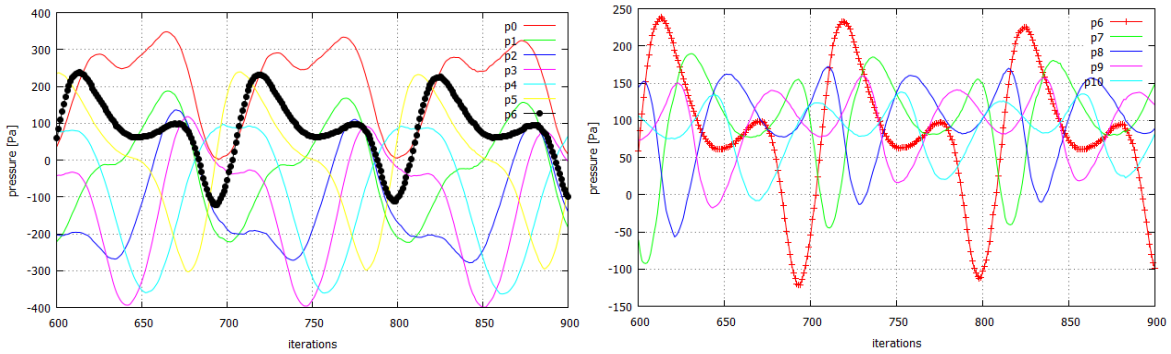

Figure 14. Pressure evolution for case F2 along the diaphragm at points p0,…p6 (left) and p6,…p10 (right).

5 CONCLUSIONS

A millimeter-scale energy harvesting device proposed in the literature was used herein. It exploits vortex shedding behind bluff bodies in order to cause oscillations to a flexible diaphragm and convert flow energy to electrical by the piezoelectric phenomenon. Different bluff body shapes located in a flow channel were simulated by means of CFD to predict the vortex shedding severity in terms of the unsteady pressure evolution. The conclusions from this study are that the shape of the body is very important to achieve significant pressure variations and the design of the whole configuration (how many bluff bodies, in what arrangement, where to install the flexible diaphragm) is very crucial in order to finally harvest significant amounts of energy. Future work on the topic refers to design optimization of the bluff body shape and diaphragm location, consideration of fluid structure interaction in the simulations, full modelling of the whole operation using piezoelectric modelling and attempt to correlate flow energy harvesting with the electric power generated in the context of the model.

ACKNOWLEDGEMENT

The authors would like to acknowledge Mr Evangelos Karvelas, postgraduate student in the TEI of Athens, for his valuable help with the grid generation for the cases used in this paper.

REFERENCES

[1] Zhou, G., Huang, L., Li, W. and Zhu, Z. (2014), “Harvesting ambient environmental energy for wireless sensor networks: A survey (Review article)”, Journal of Sensors, Vol. 2014, 20 pages, (available in http://dx.doi.org/10.1155/2014/815467).
[2] Holmes, A.S., Hong, G. and Pullen, K.P. (2005), “Axial-flux permanent magnet machines for micropower generation”, Journal of Microelectromechanical Systems, Vol. 14, pp. 54-62.
[3] Lyshevski, S.E. (2011), “High-power density miniscale power generation and energy harvesting systems”, Energy Conversion and Management, Vol. 52, pp. 46-52.
[4] Nguyen, H-D.T Pham, H-T. and Wang D-A. (2013), “A miniature pneumatic energy generator using Karman vortex street”, Journal of Wind Engineering and Industrial Aerodynamics, Vol. 116, pp. 40-48.
[5] Akaydin, H.D., Elvin, N and Andreopoulos, Y. (2010), “Wake of a cylinder: a paradigm for energy harvesting with piezoelectric materials”, Experiments in Fluids, Vol. 49, pp. 291-304.
[6] Allen, J.J. and Smits, A.J. (2001), “Energy harvesting eel”, Journal of Fluids and Structures, Vol. 15, pp. 629-640.
[7] Sanchez-Sanz, M. Fernandez, B. and Velazquez, A. (2009), “Energy-harvesting microresonator based on the forces generated by the Karman street around a rectangular prism”, Journal of Microelectromechanical Systems, Vol. 18, pp. 449-457.
[8] Venugopal, A., Agrawal, A. and Prabhu, S.V. (2010), “Influence of blockage and upstream disturbances on the performance of vortex flowmeter with wall pressure measurement”, Measurement, Vol. 43, pp. 603-616.
[9] Miau, J.J. and Liu, T.W. (1990), “Vortex flowmeter designed with wall pressure measurement”, Review of Scientific Instruments, Vol. 61, pp. 2676-2681.
[10] Fu, X. and Yang, H. (2001), “Study of hydrodynamic vibrations in dual bluff body vortex flowmeter”, Chinese Journal of Chemical Engineering, Vol. 9, pp. 123-128.
[11] Peng, J. Fu, X. and Chen, Y. (2004), “Flow measurement by a new type vortex flowmeter of dual triangulate bluff body”, International Journal of Energy Research, Vol. 33, pp. 1180-1190.